GT2011-45191

SIMULATIONS OF MULTI-PHASE PARTICLE DEPOSITION ON A SHOWERHEAD WITH STAGGERED FILM-COOLING HOLES

Seth A. Lawson and Karen A. Thole
The Pennsylvania State University
Department of Mechanical and Nuclear Engineering
University Park, PA, USA

Yoji Okita and Chiyuki Nakamata
IHI Corporation
Aero-engine & Space operations
229, Tonogaya, Mizuho-machi, Nishitama-gun, TOKYO, JAPAN

ABSTRACT

The demand for cleaner, more efficient energy has driven the motivation for improving the performance standards for gas turbines. Increasing the combustion temperature is one way to get the best possible performance from a gas turbine. One problem associated with increased combustion temperatures is that particles ingested in the fuel and air become more prone to deposition with an increase in turbine inlet temperature. Deposition on aero-engine turbine components caused by sand particle ingestion can impair turbine cooling methods and lead to reduced component life. It is necessary to understand the extent to which particle deposition affects turbine cooling in the leading edge region of the nozzle guide vane where intricate showerhead cooling geometries are utilized.

For the current study, wax was used to dynamically simulate multi-phase particle deposition on a large scale showerhead cooling geometry. The effects of deposition development, coolant blowing ratio, and particle temperature were tested. Infrared thermography was used to quantify the effects of deposition on cooling effectiveness. Although deposition decreased with an increase in coolant blowing ratio, results showed that reductions in cooling effectiveness caused by deposition increased with an increase in blowing ratio. Results also showed that effectiveness reduction increased with an increase in particle temperature. Reductions in cooling effectiveness reached as high as 36% at M = 1.0.

NOMENCLATURE

A   surface area
C   particle specific heat
C_D film-cooling hole discharge coefficient
C_p pressure coefficient, $C_p = (p - p_\infty)/(2\rho_\infty U_\infty^2)$
Δh_{fus} specific latent heat of fusion
d   film-cooling hole diameter, d = 1.24 cm
D   cylinder outside diameter
d_p particle diameter
DR   density ratio, $DR = \rho_c/\rho_\infty$

h   heat transfer coefficient
I   momentum flux ratio, $I = \rho_c U_c^2/\rho_\infty U_\infty^2$
k   thermal conductivity
L   film-cooling hole length
L_c characteristic length for Stokes number
L_p particle travel distance
M   average film-cooling blowing ratio, $M = \rho_c U_c/\rho_\infty U_\infty$
M_L local blowing ratio, $M_L = \rho_c C_D \sqrt{2(p_c - p_{\infty,1})/\rho_c}/\rho_\infty U_\infty$
p   static pressure
Re_D cylinder Reynolds number, $Re_D = \rho_\infty U_\infty D/\mu$
Re_p particle Reynolds number, $Re_p = \rho_\infty U_p d_p/\mu$
s   circumferential distance from stagnation
Stk   Stokes number, $Stk = \rho_p d_p^2 U_p/18\mu L_c$
T   temperature
TSP   thermal scaling parameter of median sized particle
U   velocity
V   volume
VR   velocity ratio, $VR = U_c/U_\infty$
x   streamwise distance from stagnation
y   pitchwise distance from stagnation
z   spanwise distance from base of cylinder

Greek

η_{aw} adiabatic effectiveness, $\eta_{aw} = (\eta_{meas} - \eta_{min})/(1 - \eta_{min})$
η_{meas} measured effectiveness, $\eta_{meas} = (T_\infty - T_{aw})/(T_\infty - T_c)$
η_{min} minimum measured effectiveness
$\overline{\eta}$ spanwise-averaged effectiveness
$\overline{\overline{\eta}}$ area-averaged effectiveness
$\overline{\overline{\eta}}_o$ baseline area-averaged effectiveness (no deposition)
ρ density
μ gas dynamic viscosity
θ angle from stagnation

Subscripts

aw   adiabatic wall
c   coolant
i   initial
l   local
p   particle
s   solidification
w   wax
∞ mainstream

INTRODUCTION

A major challenge of gas turbine design is developing methods to cool turbine components so that higher combustion temperatures and thus better performance can be achieved. Sophisticated film-cooling geometries must be effectively designed to provide the maximum cooling for the minimum cost to engine efficiency.

To make matters worse, particles in the hot gas path can deposit on turbine components. The particulate matter can come from impurities in the fuel or from airborne particulates such as sand or volcanic ash. Ideally, particles in the air and fuel supply would be filtered prior to entering the combustor. For aero engine applications, no such filters exist and sand particles on the order of 10 μm have been found to deposit on turbine components directly downstream of the combustor [1]. The resulting particle deposition has been found to have a dramatic effect on turbine component life. The section of the turbine most sensitive to heat transfer from the hot gas path is the leading edge of the nozzle guide vane. A dense series of cooling holes arranged at different incidence angles around the circumference of the vane leading edge is often utilized to ensure proper cooling of the high heat transfer region. These cooling geometries used around the leading edge region are often referred to as showerhead geometries. A better understanding of the effects of deposition in the vicinity of showerhead cooling geometries is required to ensure that cooling designs can withstand the effects of deposition.

For the current study, a novel approach was utilized to dynamically simulate sand deposition in aero engines to determine its effects on a showerhead cooling geometry. Low melting temperature wax was used as the particulate to simulate deposition on a large scale showerhead model. Experiments were conducted to test the effects of key parameters such as coolant blowing ratio and particle temperature on deposition and the resulting cooling effectiveness. Infrared (IR) thermography was used to measure surface temperatures and quantify cooling effectiveness before and after deposition.

REVIEW OF RELEVANT LITERATURE

The leading edge of the inlet guide vane experiences high heat transfer and requires extensive film cooling with multiple rows of holes surrounding stagnation in the form of a showerhead. Polanka et al. [2] were the first to perform highly spatially-resolved adiabatic effectiveness measurements in a showerhead cooling configuration on a nozzle guide vane model. They concluded that the showerhead performed best at high blowing ratios when cooling jets merged with adjacent jets resulting in uniform distribution of coolant around stagnation. Ou and Rivir [3] and Gao and Han [4] experimentally modeled the showerhead region using symmetric cylinder models. Both studies confirmed the conclusions by Polanka et al. [2] that cooling effectiveness improves with an increase in blowing ratio; however, Gao and Han [4] found that effectiveness decreases in the downstream region at high blowing ratios due to high mixing with the mainstream.

Deposition in turbomachinery from ingestion of foreign particles, such as sand, into the engine intake is highly dependent on factors such as combustion temperature and particle melting temperature. Experiments conducted by Wenglarz and Fox [5], Richards et al. [6], and Wenglarz and Wright [7] explored the effects of gas and surface temperatures on deposition in turbomachinery. Wenglarz and Fox [5] found that an increase in gas temperature resulted in an increase in the number of molten particles that deposit upon impaction of a turbine surface. Richards et al. [6] found that deposition rates on a surface could be decreased by increasing cooling near the surface. The increased cooling near the surface served to cool particles to a solid state preventing them from sticking to the surface upon impaction. Wenglarz and Wright [7] concluded that the gas temperature relative to the solidification temperature of a particle was the relationship that best determined the deposition probability of a particle.

Deposition was simulated in a true scale vane cascade by Smith et al. [8]. They found that deposition was sensitive to location on the vane, inlet gas temperature, and film cooling flowrate. Deposition was most dense on the leading edge and pressure surface and decreased with an increase in film-cooling flowrate.

Lawson and Thole [9] used wax to simulate deposition dynamically in the vicinity of a row of film-cooling holes on a flat plate. They found that deposition reduced cooling effectiveness by as much as 25% at low blowing ratios and only 6% at high blowing ratios. Lawson and Thole [9] determined that the effect of deposition on effectiveness reached an equilibrium state at which point, additional deposition on the film-cooled surface did not cause further reduction in cooling effectiveness. Low melting temperature wax was used by Albert et al. [10] to simulate deposition dynamically on a showerhead film-cooling geometry. They found that deposition thickness increased with time until reaching a quasi-steady state. Albert et al. [10] concluded that blowing ratio and the relationship between gas and particle solidification temperatures had large effects on deposition.

Lawson and Thole [11] used an improved wax deposition method to simulate deposition in a large scale turbine cascade to explore the effects of blowing ratio and particle phase on an endwall film cooling geometry in a large scale vane cascade. They developed a thermal scaling parameter (TSP) which they used to scale the phase of the wax particles in the mainstream gas path. They found that deposition rate increased and cooling effectiveness decreased with an increase in particle temperature causing a reduction in effectiveness by as much as 31%.

Sreedharan and Tafti [12] performed a computational study to model deposition on a showerhead film cooling geometry. They modeled the deposition and erosive behavior of 5 μm and 7 μm ash particles. They assumed that particles above their softening temperature would stick to the surface upon impaction and particles below their softening temperature

would not stick. They found that showerhead cooling holes were effective at preventing deposition, because they effectively solidified particles and diverted their trajectories. Results showed that an increase in blowing ratio increased deposition of 5 μm particles by 4% but decreased deposition of 7 μm by 5%. Although Sreedharan and Tafti [12] showed that coolant jets can reduce deposition, Albert et al. [10] concluded that secondary vortices associated with coolant jets can actually enhance particle transport to some regions of the surface.

The objective of the current study was to apply the methods used by Lawson and Thole [11] to simulate deposition on a showerhead film-cooling geometry using wax. Although a similar method was used by Albert et al. [10] to simulate deposition on a showerhead, the emphasis of their study was to determine the effects of deposition on local overall effectiveness rather than surface cooling effectiveness. For the current study, highly detailed surface temperatures were measured using IR thermography to quantify the effects of deposition development, blowing ratio, and TSP on cooling.

EXPERIMENTAL METHODS

The following section describes the experimental methods for simulating deposition and measuring the effects of deposition on showerhead film cooling effectiveness. An explanation of the facility is followed by a description of the technique used to simulate deposition and the methods used to quantify cooling effectiveness. The procedures used to simulate deposition and quantify effectiveness were similar to the methods used by Lawson and Thole [11].

Experiments for the current study were conducted in a low speed wind tunnel. Flow through the low speed wind tunnel, shown in Figure 1, is supplied by a 37kW axial fan. Downstream of the fan, the flow was cooled by a primary heat exchanger before splitting into two coolant flow paths and a mainstream flow path. The mainstream flow passed through a series of resistance heaters which heated the flow to 315K while the coolant flow paths passed through secondary heat exchangers which cooled the coolant flow to 290K. It is important to note that only the top coolant flow path was active for the current study. Downstream of the heater bank, the mainstream flow passed through a series of flow straightening screens and honeycomb. Downstream of the flow conditioning, the flow passed through a turbulence grid to create 4% turbulence intensity with a length scale of 0.16D in the mainstream flow at stagnation [13]. The leading edge film-cooling holes were located well outside of the approaching boundary layer which had a measured thickness of 7.2% of the cylinder span.

For the current study, a showerhead cooling geometry was modeled using a cylindrical test piece with a symmetric aft body airfoil. The cylinder was placed in the mainstream flow channel having a width of 8.8D resulting in a blockage ratio of 0.11. For the purpose of this study, blockage effects were assumed to be negligible considering the low blockage ratio. The symmetric aft body airfoil was added to prevent wake shedding from the cylinder which could affect the flow physics in the showerhead cooling region. Figure 2 illustrates the showerhead cooling configuration modeled with the cylindrical test piece and aft body airfoil.

Mainstream flow conditions were scaled by matching the cylinder Reynolds number between engine and laboratory conditions. Because experiments were conducted in a low speed wind tunnel, the cylindrical test piece was scaled up to match the Reynolds number. The film-cooling operating conditions were scaled using the average blowing ratio of the coolant to mainstream flow. An auxiliary blower was used to supply coolant from the upper coolant flow path to the cylindrical test piece. A laminar flow element located in the coolant flow path upstream of the cylindrical test piece was used to measure the coolant flowrate which could be adjusted using the variable speed blower. The local blowing ratio, M_L, was calculated at each cooling row location using the theoretical pressure distribution around a circular cylinder and assuming a constant discharge coefficient, $C_D = 0.6$ [14]. Although the value of C_D depends on internal and external flow conditions as well as cooling hole orientation, using an average value was adequate for the purpose of qualitative analysis in this study. Table 1 shows the geometric specifications and operating conditions used to scale the engine conditions to the laboratory model. Highlighted items in Table 1 indicate parameters that were matched to engine conditions. The showerhead geometric specifications and corresponding engine operating conditions were provided by the industry sponsor [1].

A top and side view of the flow channel with the cylindrical test piece location and velocity measurement points are shown in Figure 3. The mainstream velocity profile, shown in Figure 3a, was measured using a pitot-static probe at five locations across the span of the channel upstream of the cylindrical test piece. Pressure taps were installed in the cylinder surface near stagnation to verify that flow around the leading edge was symmetric. Figure 4 shows the dimensionless pressure distribution near stagnation compared to the theoretical pressure distribution around a circular cylinder.
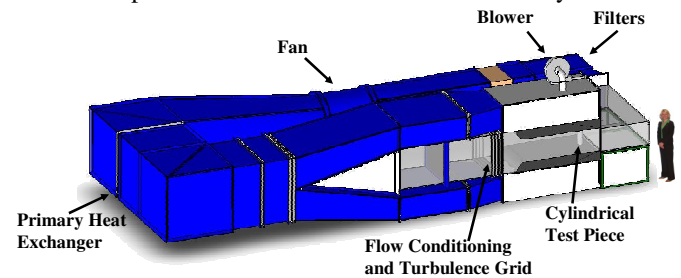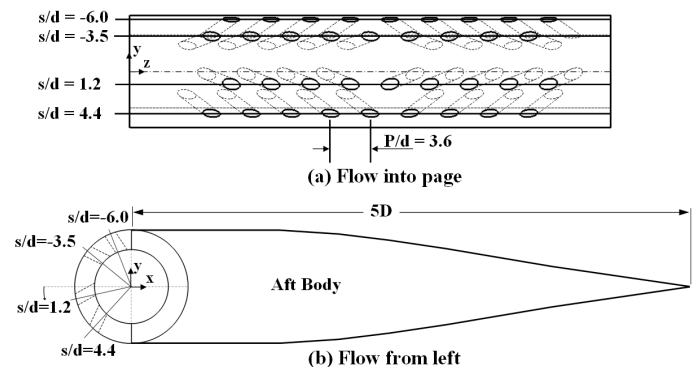

Figure 1. Illustration of wind tunnel facility.

Figure 2. Schematic illustrating the cylindrical leading edge and aft body dimensions.

Table 1. Geometry and Operating Conditions

	Nomen.	Engine [1]	Lab
density ratio	DR	1.9	1.1
blowing ratio	M	0.50 - 1.80	0.50 - 1.80
momentum flux ratio	I	0.13 - 1.71	0.23 - 3.05
velocity ratio	VR	0.26 - 0.95	0.46 - 1.68
hole incidence angle (deg)	α	40.00	40.00
hole pitch to diameter ratio	P/d	3.6	3.6
hole length to diameter ratio	L/d	2.8	2.8
Reynolds number based on D	Re_D	56800	56800

Figure 3. Schematic showing (a) measured velocity profile, (b) test section top view, and (c) test section side view.

Figure 4. Measured and theoretical dimensionless pressure distributions around the cylinder leading edge.

Dynamic Deposition Simulation and Analysis

For each experimental condition in the current study two tests were conducted. First, deposition was dynamically simulated by injecting atomized wax into the mainstream flow upstream of the cylindrical test piece. Following deposition simulation, an adiabatic effectiveness experiment was conducted to quantify the effect of deposition on cooling effectiveness. The details of the adiabatic effectiveness measurement methods are discussed in the next subsection.

To simulate deposition, atomized wax was injected using the wax particle generator illustrated in Figure 5. The wax particle generator was similar to the one used by Lawson and Thole [11] with one nozzle instead of two. Liquid wax and atomizing air were supplied to an atomizing nozzle installed in the turbulence grid located 2 m upstream of the cylindrical test piece.

The Stokes number was used to scale the particle inertial characteristics from the engine to the laboratory model. The Stokes number, defined in the nomenclature, is the non-dimensional inertial response time of a particle. Particles having high Stokes numbers are ballistic and less likely to follow streamlines around an obstacle than small particles with low Stokes numbers. An analysis was conducted to determine that wax particles with a median diameter of 175 μm in the wind tunnel test conditions would match the Stokes numbers of sand particles with a median size of 8 μm that exist in aero engine conditions. Particle Reynolds numbers calculated for engine conditions and laboratory conditions showed that the same particle flow regime could be achieved in each setting. To control the wax particle size distribution that could be generated using the system in Figure 5, the atomizing air pressure and liquid wax pressure could be independently adjusted. The liquid wax pressure determined the flowrate of wax while the atomizing air pressure could be adjusted independently to control the size of the generated particles. For a given wax flowrate particle size decreased with an increase in atomizing air pressure. For a given atomizing air pressure particle size increased with an increase in wax flowrate as illustrated in Figure 6.

A Malvern particle analyzer capable of characterizing aerosol droplets in the size range of 0.1 to 2000 μm was used to measure the size distribution of generated wax particles. Measurements were acquired 15 cm downstream of the nozzle at various vertical locations within the atomized spray. Results from different vertical measurement locations were in good agreement implying little dependence on measurement location relative to injection location. To generate particles in the size range of 175 μm, an atomizing air pressure of 70 kPa and a liquid wax pressure of 380 kPa were used. Figure 6 shows particle size distributions generated through a range of liquid wax pressures at an atomizing air pressure of 70 kPa. Measurements showed that for a given atomizing air pressure, the size distribution of particles increased with an increase in liquid wax pressure. The median particle sizes generated for each liquid wax pressure are listed in the legend of Figure 6.
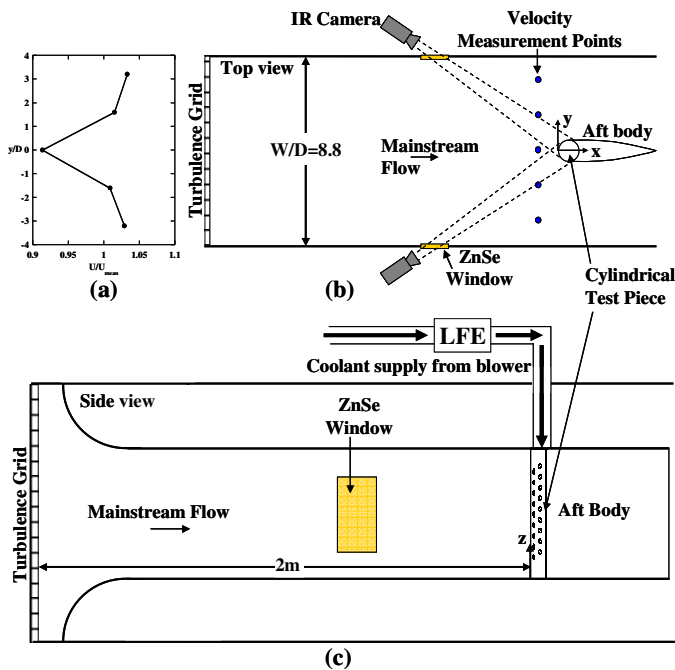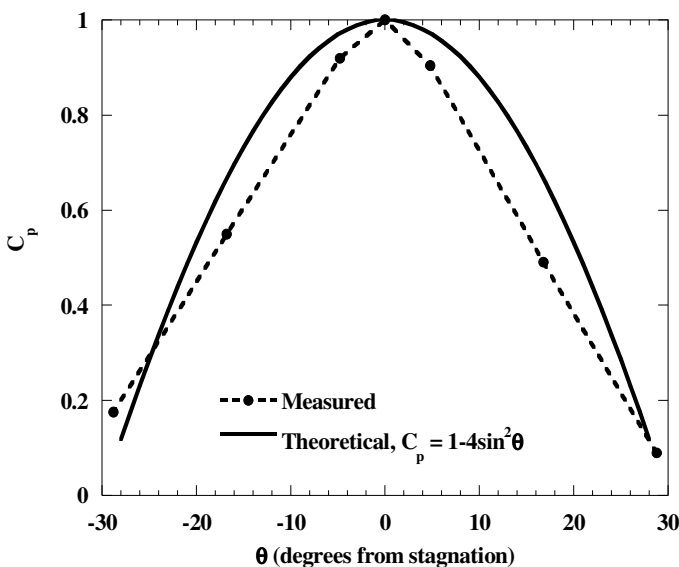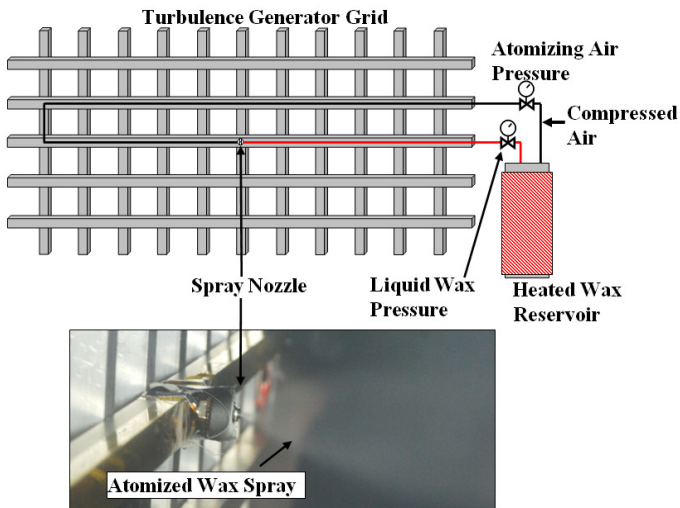
4

Figure 5. Wax particle generator and photograph of injection nozzle.

Figure 6. Particle size histograms at an atomizing air pressure of 70kPa and various liquid wax pressures.

Table 2. Particle Properties and Scaling Parameters

	Nomen.	Engine	Lab
median particle diameter (μm)	d_p	8 [1]	175
particle density (kg/m³)	ρ_p	2650 [15]	800
particle initial temperature (K)	$T_{p,i}$	2594 [1]	364
particle specific heat (J/kgK)	C_p	420 [15]	2090
particle latent heat of fusion (J/kg)	Δh_{fus}	142000 [15]	225600
particle solidification temperature (K)	T_s	1972 [15]	351
particle solidification time (t_s)	t_s	1.25×10^{-4}	0.17
particle velocity (m/s)	U_∞	140 [1]	6.68
particle travel distance (m)	L_g	0.147 [1]	2.05
particle Reynolds number	Re_p	80	80
thermal scaling parameter	TSP	0.12	1.0/2.0
Stokes number	Stk	4.00	4.00

Results from the literature have shown that the phase of the particle upon impacting a surface is the most important characteristic that determines whether or a not a particle will deposit on that surface. To scale the thermal characteristics of sand particles in the engine to wax particles in the lab, a thermal scaling parameter (TSP), developed by Lawson and Thole [11], was used. The TSP is essentially a dimensionless solidification time of a particle immersed in a flow assuming

the particle is a lumped mass and that it is traveling at the same velocity as the surrounding flow. To calculate the TSP, the solidification time of the particle is normalized by the time it takes the particle to travel from the injection location to the surface of interest. In an engine, the travel time would be equivalent to the time it takes a particle to travel from the combustor to the nozzle guide vane. Theoretically, particles having TSP values less than one are in solid form upon reaching the nozzle guide vane while particles having TSP values greater than one are in molten form upon reaching the nozzle guide vane. A detailed discussion of the TSP is presented by Lawson and Thole [11].

Because the TSP is highly sensitive to particle diameter, the TSP of the median particle size was used to characterize the particle phase. In laboratory conditions, TSP is sensitive to particle injection temperature, particle solidification temperature, and mainstream flow temperature all of which can be adjusted independently to achieve the necessary TSP to match engine conditions. To simulate deposition, microcrystalline wax with a solidification temperature of 351 K was used to simulate deposition. To achieve TSP = 1.0, wax was injected into the mainstream with T_∞ = 290 K. To achieve TSP = 2.0, wax was injected into the mainstream with T_∞ = 317 K. Table 2 shows the particle material properties, operating conditions, and particle scaling parameters for sand particles in the actual engine compared to wax particles in the laboratory wind tunnel.

Following each deposition simulation, photographs were taken to further analyze the deposition area coverage using the methods described by Lawson and Thole [11]. In addition to measuring surface area coverage, deposition thickness
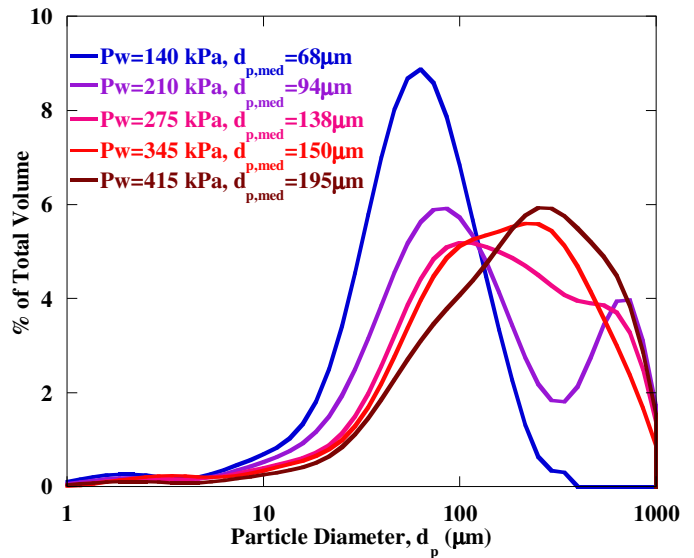
measurements were made at various spanwise and circumferential locations on the cylindrical surface. Deposition thickness measurements were made using a depth gage typically accurate to within 2 mm (0.16d). The resulting surface with deposition was painted with flat black paint to create uniform surface emissivity so that surface temperatures could be measured accurately using IR thermography as described in the following subsection.

Adiabatic Effectiveness Measurements

Steady state IR thermography experiments were conducted to quantify film-cooling effectiveness at various operating conditions with and without deposition. Surface temperatures were measured using a FLIR SC620 IR camera with a spectral range of 7.5 μm to 13 μm. Using the IR camera allowed for high resolution measurements compared to conventional techniques in which measurement resolution is limited by the number of thermocouples mounted on a surface. The IR camera used in the current study had measurement resolution of 1.36 pixels/mm (17.3 pixels per hole diameter).

Thermocouples were used to measure mainstream and coolant temperatures which were monitored to determine when a steady state was achieved for each experiment. Upon

reaching steady state, five IR images from two separate port locations, shown in Figure 3, were acquired to obtain a temperature map around the leading edge circumference of the cylindrical test piece. Zinc Selenide windows were used at each port location to prevent mainstream leakage flow through the IR image ports.

Four thermocouples used for IR image calibration were mounted in hot and cold locations on the cylindrical surface. Each IR image was calibrated by adjusting emissivity and background temperature until the IR measurements matched the respective calibration thermocouple measurements. The five calibrated IR images from each port location were then averaged to yield one data set from each port location.

Because the surface of interest was curved, each calibrated data set required spatial transformation. Prior to running experiments, a 12.7 x 12.7mm grid was placed on the cylindrical surface and an IR image of the grid was acquired at each camera port location. The grid point locations were then identified and the data was effectively unwrapped from the curved surface so that the data around the curved surface could be represented on a plot with rectangular coordinates. The transformation algorithm developed by Colban et al. [16] was used to transform the data from every ensuing experiment.

Following image transformation, measured adiabatic effectiveness, η_{meas}, was calculated at every pixel location in the IR data set. After calculating the measured adiabatic effectiveness, each resulting matrix of measured effectiveness values were corrected to account for the heat loss through the foam wall. Although the foam had a relatively low thermal conductivity (k=0.037W/mK) it was not a purely adiabatic surface. A one-dimensional conduction correction was implemented to account for the heat loss through the foam wall to the coolant plenum inside the cylinder. To correct for the heat loss through the foam cylinder wall, the final corrected effectiveness values, η_{aw}, were calculated using the equation in the nomenclature, where η_{min} is the equivalent effectiveness attributable to heat loss through the cylinder wall. The value for η_{min} was equal to the minimum η_{meas} value for every experiment. The minimum measured effectiveness value for each case was in a region on the cylinder surface where the only measured effectiveness was that which was attributable to conduction losses through the cylinder wall.

Uncertainty Analysis

The uncertainty propagation method described by Moffat [17] was used to perform an uncertainty analysis for the blowing ratio and adiabatic effectiveness calculations in the current study. The blowing ratio uncertainty was ±0.021 at M = 0.5 (4.2%) and 0.026 at M = 1.8 (1.43%). The bias uncertainty for thermocouples that were used to measure coolant jet and mainstream temperatures was 0.5°C while the precision uncertainty for thermocouple measurements was 0.06°C. The total bias and total precision uncertainties associated with the IR measurements were 0.57°C and 0.16°C respectively. Adiabatic effectiveness uncertainty was ±0.024 at $\eta_{aw} = 0.07$ and ±0.026 at $\eta_{aw} = 0.73$.

DISCUSSION OF RESULTS

For the current study, a test matrix was developed to test the effects of deposition on film-cooling at two TSP values and three blowing ratios. To determine the effects of deposition on film-cooling, experiments were first conducted to determine the quantity of injected wax necessary for the deposition to reach an equilibrium state. Lawson and Thole [9] concluded that the effects of deposition on a film-cooled flat plate reached an equilibrium state at which point additional deposition buildup on the surface no longer affected cooling effectiveness. Albert et al. [10] observed that deposition reached an equilibrium state on a leading edge model. For the current study, multiple tests with different wax injection durations were conducted at M = 1.0 to determine the proper injection duration to reach the equilibrium state. It is important to note that for each condition tested, a deposition simulation test as well as an adiabatic effectiveness measurement experiment was conducted.

Prior to deposition simulation, a set of baseline adiabatic effectiveness experiments were conducted. Figure 7 shows the baseline adiabatic effectiveness contour plots at each blowing ratio tested. An interesting finding from the baseline tests is that the row of holes closest to stagnation at s/d = 1.2 ejects no coolant at the lowest blowing ratio. There is no coolant ejecting from the s/d = 1.2 row at M = 0.5 because of the high pressure region near stagnation. The s/d = 1.2 hole locations are illustrated by the blue ellipses in Figure 7a. As the blowing ratio was increased to M = 1.0 coolant began to exit the s/d = 1.2 row and provided good coolant coverage around the circumference of the leading edge. As the blowing ratio was increased further to M = 1.8, the coolant jets separated from the surface and the total surface coolant coverage decreased. Table 3 lists the local blowing ratios at each row of holes for each cooling condition.

Figure 8 shows the spanwise-averaged cooling effectiveness relative to circumferential location (s/d) near the leading edge showerhead region. The location of the center of each cooling row is shown by dashed lines in Figures 7a and 8. The general trend of the data shows that peak effectiveness increased with an increase in blowing ratio; however, because the coolant jets are separated at M = 1.8, the effectiveness between holes was highest at M = 1.0. The exception to this trend is the row of holes located at s/d = -6.0. For the row at s/d = -6.0, the blowing ratio exhibiting the highest peak effectiveness as well as the highest surrounding effectiveness was M = 0.5. At s/d = -6.0, the local blowing ratios at M = 0.5, 1.0, and 1.8 were M_L = 1.2, 1.4, and 2.0. The highest effectiveness probably occurred at M = 0.5 (M_L = 1.2) because separation effects reduced effectiveness as the local blowing ratio exceeded 1.2. The same thing happened at the s/d = 4.4 row. When the local blowing ratio exceeded 1.2, effectiveness decreased indicating separation.

Also shown in Figure 8 is the data reported by Polanka et al. [2] for M = 0.5 and M = 1.8 at Tu = 2.2%. Similar to the data for the current study, Polanka et al. [2] showed an increase in cooling effectiveness with an increase in blowing ratio; however, they did not observe separation at M = 1.8 because their cooling holes had a more shallow injection angle of 25° as compared to the 40° injection angle in the current study. Polanka et al. [2] also had a cooling row at stagnation that
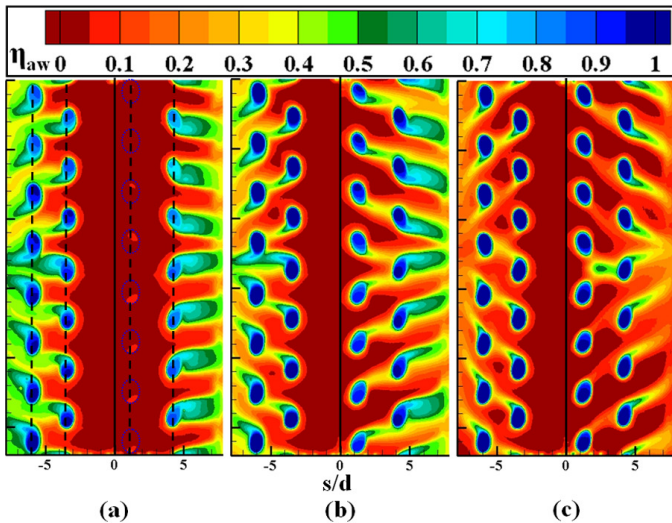
Figure 7. Adiabatic effectiveness contours at (a) M = 0.5, (b) M = 1.0, and (c) M = 1.8 with no deposition.

Table 3. Local Blowing Ratios

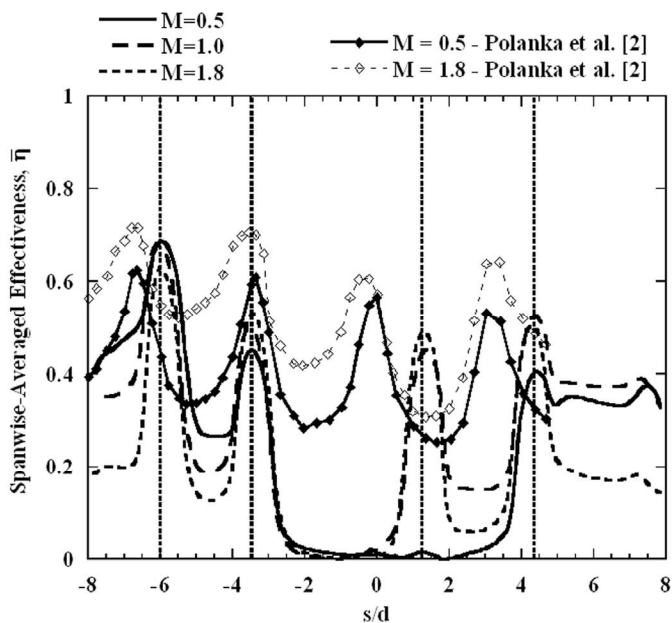| Cooling Row, s/d	M_L		
	M = 0.5	M = 1.0	M = 1.8
-6	1.2	1.4	2.0
-3.5	0.6	1.0	1.8
1.2	-0.7	0.4	1.5
4.4	0.9	1.2	1.9

Figure 8. Spanwise-averaged effectiveness for the baseline film-cooling tests with no deposition.

prevented the local minimum in effectiveness observed in the current study. Polanka et al. [2] measured higher effectiveness between cooling rows than the current study which can also be attributed to differences in geometric specifications such as injection angle.

Effects of Deposition Development

The photographs of deposition development in Figure 9 show an asymmetric deposition pattern due to the asymmetric cooling hole pattern near the stagnation region. The regions highlighted by the orange boxes in the photographs in Figure 9 have been expanded as shown in Figure 10. Deposition collected most densely around the cooling holes in the stagnation region. Particles that deposit near stagnation are the largest particles with the highest Stokes numbers and are, therefore, minimally affected by changes in the flowfield. The photographs in Figure 10 illustrate that hole blockage increases with an increase in wax injection mass.

The contours in Figure 9 show how cooling effectiveness is affected by deposition as it develops at M = 1.0 and TSP = 1.0. The impact of deposition collection can be seen in the effectiveness contours. Comparing Figures 9a and 9d, the effectiveness downstream of the s/d = 1.2 row is reduced dramatically compared to the baseline because of cooling hole blockage due to deposition.

The spanwise-averaged effectiveness plots in Figure 11 show how effectiveness changed with increased deposition across the circumference of the leading edge region at M = 1.0. An increase in deposition caused a decrease in cooling effectiveness at all rows except the row located at s/d = 4.4. Although peak effectiveness improved with deposition near the hole exit at s/d = 4.4, the deposition near the hole trailing edge prevented coolant from spreading and reduced spanwise-averaged effectiveness downstream of the row. A theory for the increase in effectiveness with deposition at s/d = 4.4 is presented in the following section.
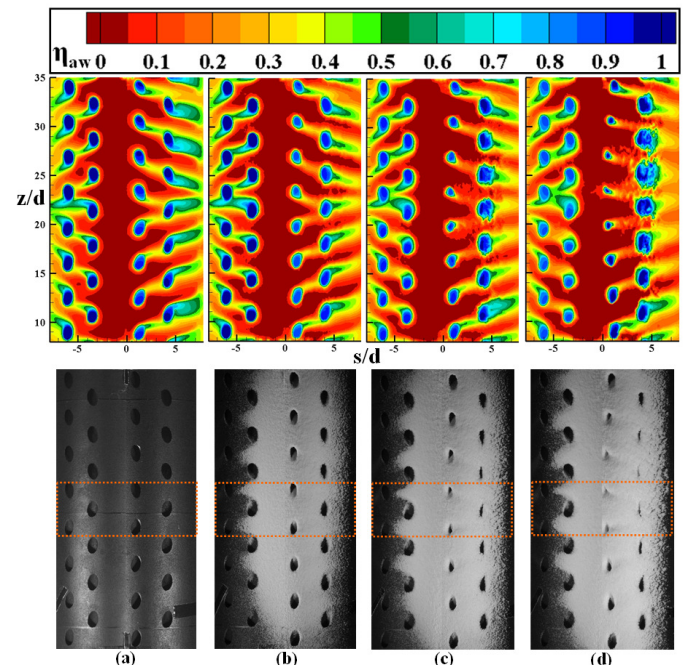

Figure 9. Adiabatic effectiveness contours and deposition photographs of the showerhead at M=1.0 (a) before deposition, (b) after 100g, (c) after 200g, and (d) after 300g of wax injection at TSP = 1.0.
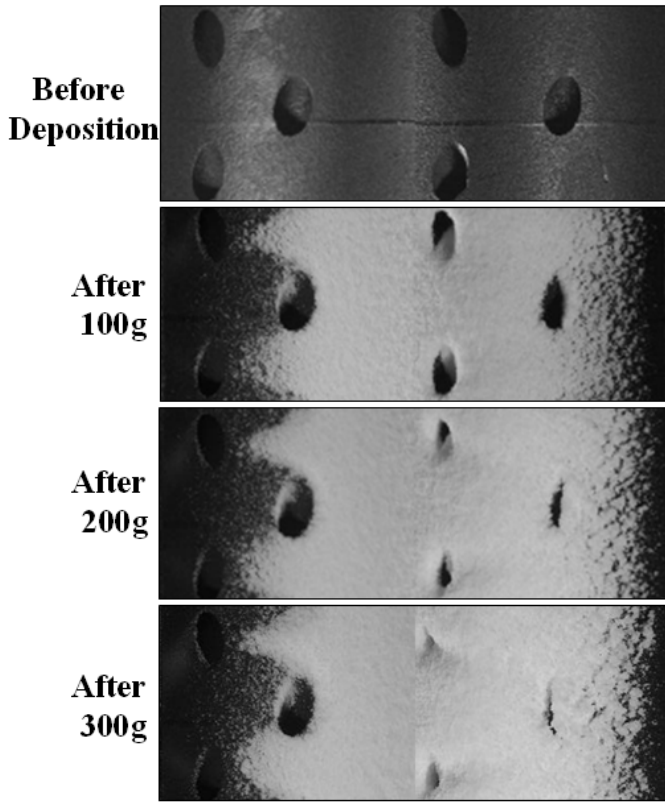
7   Copyright © 2011 by ASME

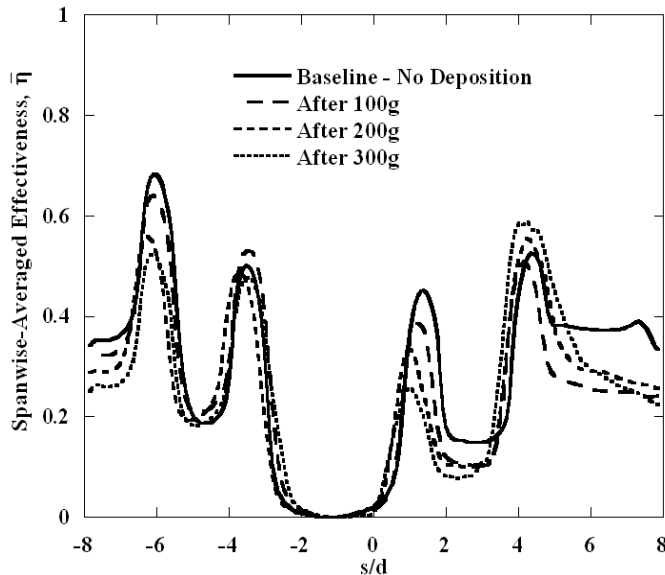**Figure 10. Enlargements of deposition photographs taken at different wax injections at M = 1.0.**

Figure 11. Spanwise-averaged effectiveness before deposition and after 100g, 200g, and 300g of wax injection at M=1.0 and TSP = 1.0.

Following each deposition test, the thickness of deposition was measured around the leading edge at three spanwise locations. Figure 12 shows the average measured thickness after 100g, 200g, and 300g at M=1.0. The plot in Figure 12 shows that thickness is on the order of a cooling hole diameter, similar to Albert et al. [10], and increases linearly with wax injection up to 300g.
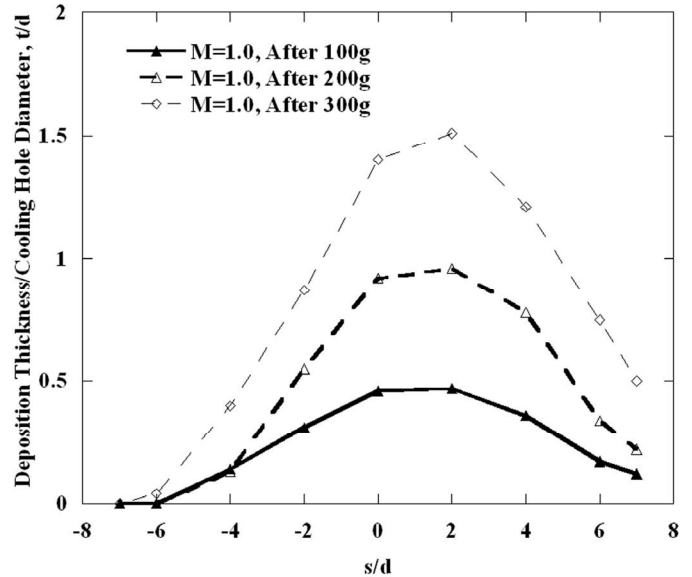
Figure 12. Average circumferential deposition depth after 100g, 200g, and 300g of wax injection at M = 1.0 and TSP = 1.0.
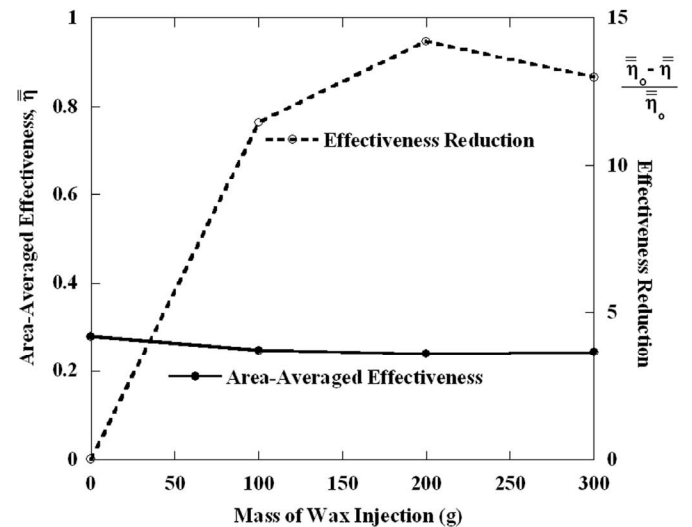

Figure 13. Area-averaged effectiveness plotted with respect to mass of injected wax at M = 1.0 and TSP = 1.0.

Area-averaged effectiveness for each case was calculated for the entire area shown in each contour. The area-averaged adiabatic effectiveness and effectiveness reduction caused by deposition are plotted relative to injection mass in Figure 13. The largest reduction in effectiveness was observed after just 200g of wax injection. Between 200g and 300g of injection, effectiveness reduction changed by less than 2%. The small change in effectiveness between 200g and 300g of wax injection justified the use of 300g of wax to capture the effects of deposition for the remaining experiments.

Effects of Blowing Ratio

Deposition experiments were conducted at blowing ratios of M = 0.5, 1.0, and 1.8. Results from the literature paint a good picture of the effects of varying blowing ratio on cooling effectiveness; however, the literature provides very few studies to help us understand how cooling may be affected by deposition at different operating conditions. The relationship

between deposition and film-cooling is a two-way coupled dependency. Not only is deposition dependent on the cooling condition, but the cooling effectiveness is dependent on the resulting deposition. Albert et al. [10] showed results to support this two-way coupling theory. They determined that deposition collected in areas downstream of cooling rows where heat transfer augmentation is typically high. They also observed deposition collection within and downstream of holes that affected the dynamics of the coolant jets. So not only was deposition affected by the coolant, the coolant was affected by the deposition.

Figure 14 shows adiabatic effectiveness contour plots before and after deposition with photographs of resulting deposition after 300g of wax injection for all three blowing ratios at TSP = 1.0. The dependence of deposition on blowing ratio can be seen clearly in the deposition photographs in Figure 14. As blowing ratio increased (left to right), the cooling hole blockage decreased. Decreased hole blockage with increased blowing occurred because jet velocity increased with increased blowing ratio and, therefore, was more effective at diverting particle trajectories. This effect of jet velocity on hole blockage is most obvious in the $s/d = 1.2$ row of holes where high external pressure prevented high jet velocities at low blowing ratios. Close-up images of deposition at mid-span for each blowing ratio are shown in Figure 15. The images in Figure 15 are close-ups of the regions indicated by the orange boxes in Figure 14c.

Deposition that occurred in the wakes of cooling holes is more complicated than deposition in the cooling holes. The wake deposition behavior can be most clearly observed downstream of the row located at $s/d = -3.5$ in Figure 15. The deposition that occurred in the wakes of the $s/d = -3.5$ row decreased with blowing ratio while the coolant jets were attached to the surface. As blowing ratio increased to $M = 1.8$, the coolant jets separated from the surface. The complex nature of the flow associated with coolant jet separation caused deposition to collect downstream of cooling holes in regions of high vorticity. The effect of jet separation on deposition is most obvious downstream of the $s/d = -3.5$ row in Figure 15c.

The effect of deposition on cooling is illustrated in the adiabatic effectiveness contour plots at each blowing ratio in Figure 14. Deposition collection in the $s/d = 1.2$ row of holes caused a blockage effect and decreased cooling effectiveness within and downstream of the $s/d = 1.2$ row at all three blowing ratios. At $M = 0.5$, any cooling that did exist near the $s/d = 1.2$ row was eliminated by the complete blockage of that row illustrated in Figure 15a. At $M = 1.0$, the cooling effectiveness of the $s/d = 1.2$ row was decreased dramatically by dense collection of deposition within the $s/d = 1.2$ row. At $M = 1.8$, the effect of deposition within the $s/d = 1.2$ row was not as great as at lower blowing ratios because the high jet velocities prevented dense deposition within the holes. At $M = 0.5$ and $M = 1.0$ the blockage of the $s/d = 1.2$ row caused by deposition caused coolant to be re-routed to other cooling holes improving effectiveness at those locations. This improved effectiveness is most obvious near the row located at $s/d = 4.4$ in Figure 14b at $M = 1.0$. Increased coolant to the $s/d = 4.4$ row improved effectiveness close to the hole exits; however, deposition close to the hole exit of the $s/d = 4.4$ row prevented coolant from

spreading downstream of that row as effectively as it did in the baseline case.

The direct effects of deposition on cooling can be seen in the local effectiveness reduction plot in Figure 16. It is important to note that effectiveness reduction was normalized with the area-averaged effectiveness for each corresponding baseline case. At $M = 0.5$, effectiveness reduction was negative in most locations indicating that deposition caused a slight improvement in effectiveness. The improvement can be seen at and downstream of the rows located at $s/d = -6.0$ and -3.5. At the row of holes located at $s/d = 4.4$, the peak cooling within the row improved due to deposition at $M = 0.5$ and $M = 1.0$;
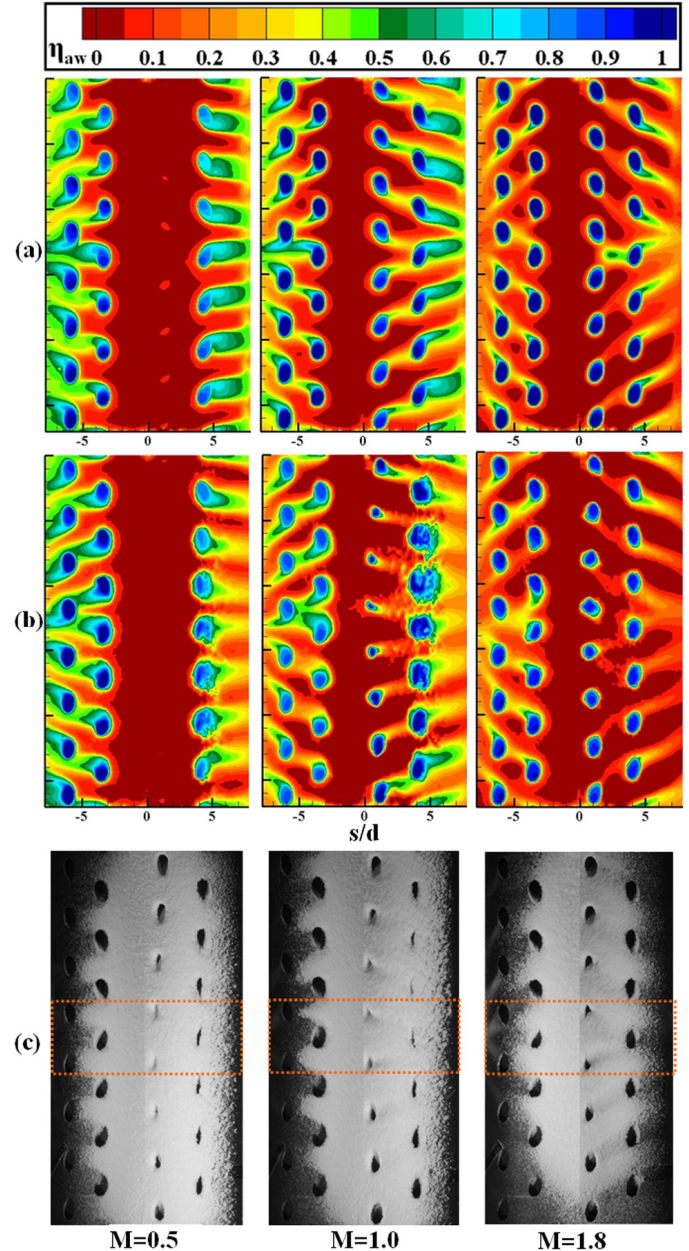

Figure 14. Adiabatic effectiveness contours (a) before deposition and (b) after 300g of wax injection at TSP = 1.0 and (c) deposition photographs at M=0.5, 1.0, and 1.8.
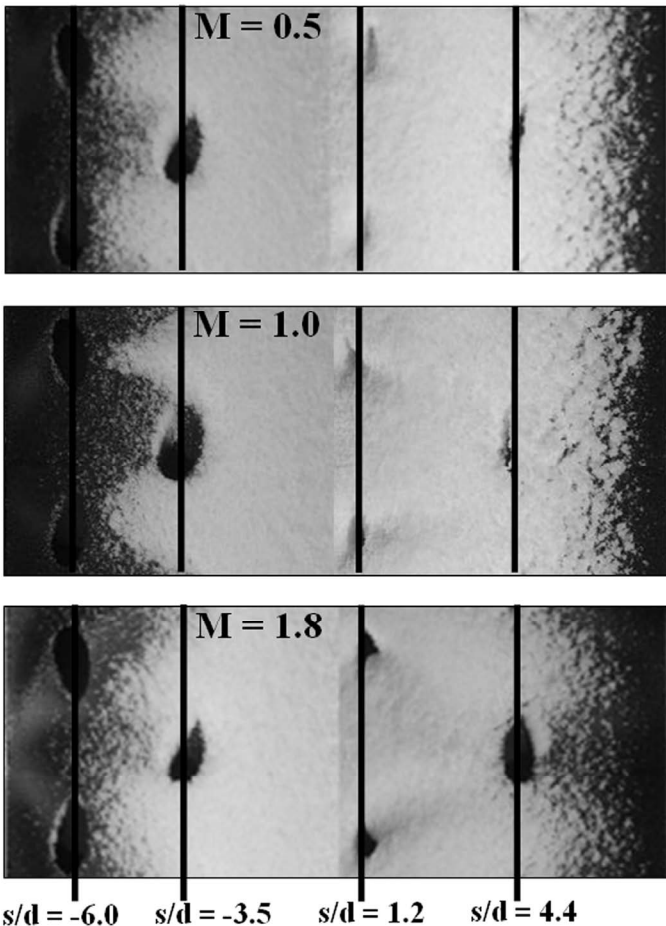
Figure 15. Mid-span deposition photographs at (a) M = 0.5, (b) M = 1.0, and (c) M = 1.8 with TSP = 1.0.

Figure 16. Spanwise-averaged local effectiveness reduction for all blowing ratios at TSP = 1.0.
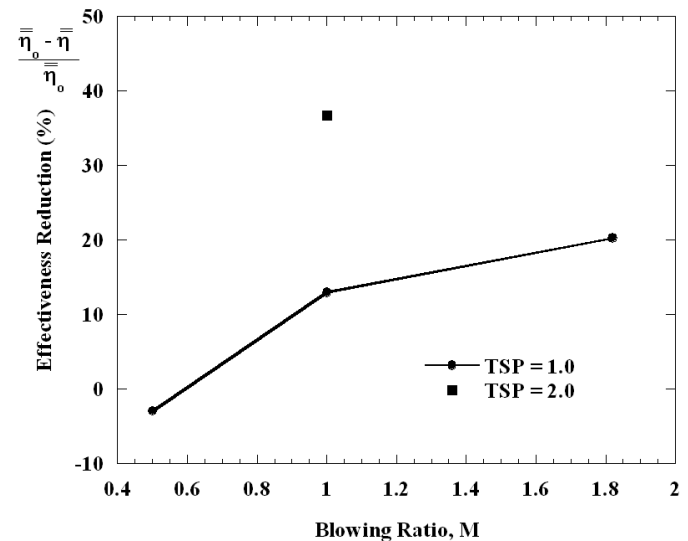
Figure 17. Effectiveness reduction with respect to blowing ratio for all cases tested.

however, as previously described, deposition near the exits of cooling holes prevented the coolant from spreading effectively downstream of the cooling row. The prevention of coolant spread at s/d = 4.4 caused a reduction in effectiveness downstream of the cooling holes at all three blowing ratios as shown in Figure 16. The maximum effectiveness reduction occurred at M = 1.0 and 1.8 just downstream of the s/d = 1.2 row. The maximum improvement in effectiveness occurred at M = 1.0 near the s/d = 4.4 row of holes.

Figure 17 shows the area-averaged effectiveness reduction caused by the deposition for each case tested. Before deposition, area-averaged effectiveness increased with blowing ratio between M = 0.5 and M = 1.0 to reach a peak value at M = 1.0. As blowing ratio increased to M = 1.8, the coolant jets separated from the surface causing a decrease in area-averaged cooling effectiveness. Deposition caused a 2.9% improvement in effectiveness at M = 0.5 while deposition reduced effectiveness by 13% at M = 1.0 and 20% at M = 1.8. Although baseline experiments showed that the maximum effectiveness occurred at M = 1.0 before deposition, the maximum effectiveness occurred at M = 0.5 after deposition. However, even though the area-averaged effectiveness was higher at M = 0.5 than at M = 1.0 after deposition, M = 1.0 may still be the best operating condition because it provided better cooling near stagnation with and without deposition as shown in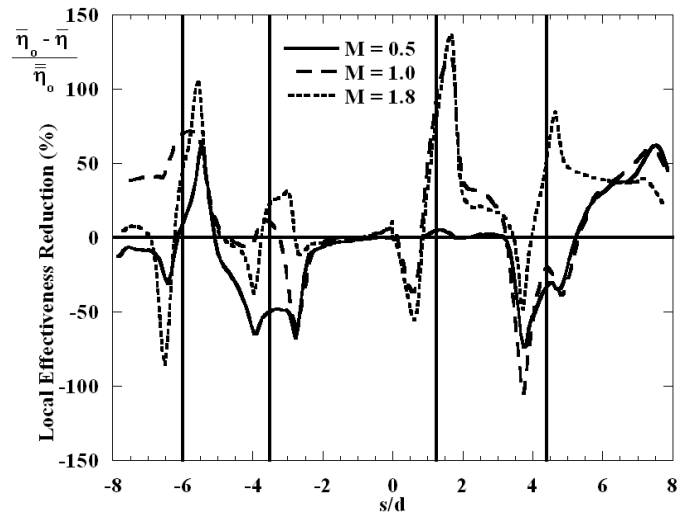 Figure 14. Because stagnation is the region of highest heat transfer from the hot mainstream, cooling conditions should be designed to provide maximum cooling to that area.

The deposition thickness relative to circumferential location for every blowing ratio tested is presented in Figure 18. As discussed previously, deposition was prevented from collecting inside cooling holes at M = 1.8 because high jet velocities diverted particle trajectories. The data in Figure 18 suggests that the high jet velocities prevented deposition from collecting at all locations around the circumference of the leading edge, not just local to the cooling holes. Of the blowing ratios tested, the thickest deposition occurred at M=1.0 near s/d = 2. Deposition was thickest downstream of the s/d = 1.2 row and between cooling holes. Thick ridges of deposition were formed between cooling holes because some particles that were diverted by coolant jets likely deposited between holes which is why the deposition layer was not as thick at M = 0.5 as it was at M = 1.0. At M = 0.5, the s/d = 1.2 row of cooling holes had little effect on approaching particles which resulted in a more uniform deposition layer at M = 0.5 than at M = 1.0.
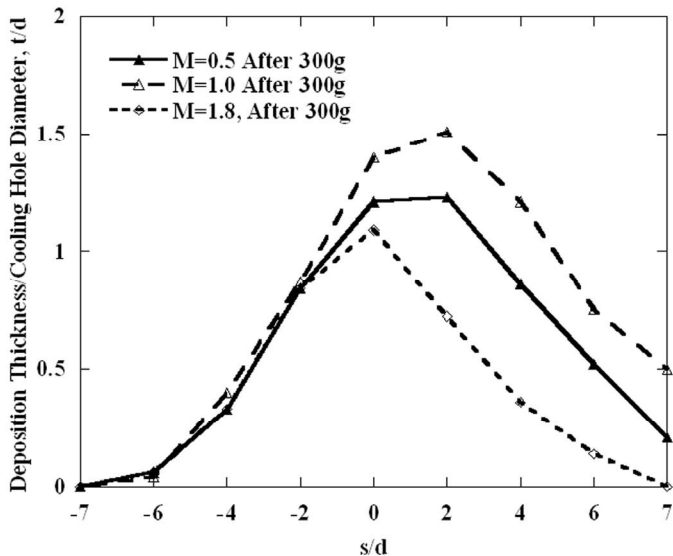
Figure 18. Non-dimensional deposition thickness at all three blowing ratios after 300g at TSP = 1.0.

Because the deposition layer was more uniform at M = 0.5, the maximum thickness was not as great at M = 0.5 as it was at M = 1.0. This effect is evident when comparing the deposition photos in Figure 15a and 15b. The deposition ridge between holes in the s/d = 1.2 row can be seen in Figure 15b. The fraction of total area covered by deposition was measured using a digital image analysis method described by Lawson and Thole [11]. The deposition area coverage at M=0.5, 1.0, and 1.8 were 79%, 77%, and 74% respectively. Deposition area coverage decreased with an increase in blowing ratio because the increase in jet velocity decreased the deposition likelihood of approaching particles. Although the deposition thickness was maximum at M=1.0, the deposition area coverage was maximum at M = 0.5 and decreased with an increase in blowing ratio.

Effects of Thermal Scaling Parameter

Deposition in engine conditions is highly dependent on factors such as combustion temperature and particle material properties that determine the phase of the particle upon impaction. Results in the literature have shown that deposition likelihood is highly dependent on the phase of a particle upon impaction of a surface [5-7]. The thermal scaling parameter (TSP) described in detail by Lawson and Thole [11] was developed to scale the particle phase upon impaction. To test the effects of particle phase on deposition and cooling effectiveness, experiments with TSP = 1.0 and TSP = 2.0 were conducted at M = 1.0.

Figure 19 shows the cooling effectiveness contours and surface deposition photographs for the baseline case as well as the cases with TSP = 1.0 and TSP = 2.0 at M = 1.0. Deposition area coverage was 77% at TSP = 1.0 and 83% at TSP = 2.0. Particles were more likely to stick to the surface which led to more deposition in coolant wakes at TSP = 2.0 than at TSP = 1.0. Deposition in coolant wakes is suppressed at TSP = 1.0 because the coolant solidifies entrained particles reducing their likelihood of deposition upon impaction. At TSP = 2.0, particles are sticky enough to deposit even after passing

through the coolant jet. Deposition in coolant wakes at TSP = 2.0 reduced the cooling effectiveness between cooling holes for every row of holes.

Deposition was more dense and difficult to remove from the surface at TSP = 2.0 than at TSP = 1.0. Interestingly, cooling hole blockage seemed more severe at TSP = 1.0 than at TSP = 2.0. Even though the s/d = 4.4 cooling holes appear to be more blocked at TSP = 1.0 than TSP = 2.0, they still provide better cooling at the low TSP case. The less dense deposition at TSP = 1.0 was more porous than deposition resulting from TSP = 2.0 allowing for coolant to pass through significant hole blockage at s/d = 4.4.

The spanwise-averaged effectiveness plot shown in Figure 20 illustrates that effectiveness between cooling rows decreased dramatically with an increase in TSP. The area-averaged effectiveness values at the baseline case, at TSP = 1.0, and at TSP = 2.0 were 0.280, 0.24, and 0.18 respectively. These values resulted in effectiveness reduction values of 13% and 37% at TSP = 1.0 and TSP = 2.0 respectively. It can be concluded that an increase in TSP leads to an increase in deposition rate and an increase in effectiveness reduction. This conclusion means that the improvement obtained in gas turbine performance by increasing combustion temperatures may come with a side-effect of increased particle deposition rates that can lead to reduced turbine component life.
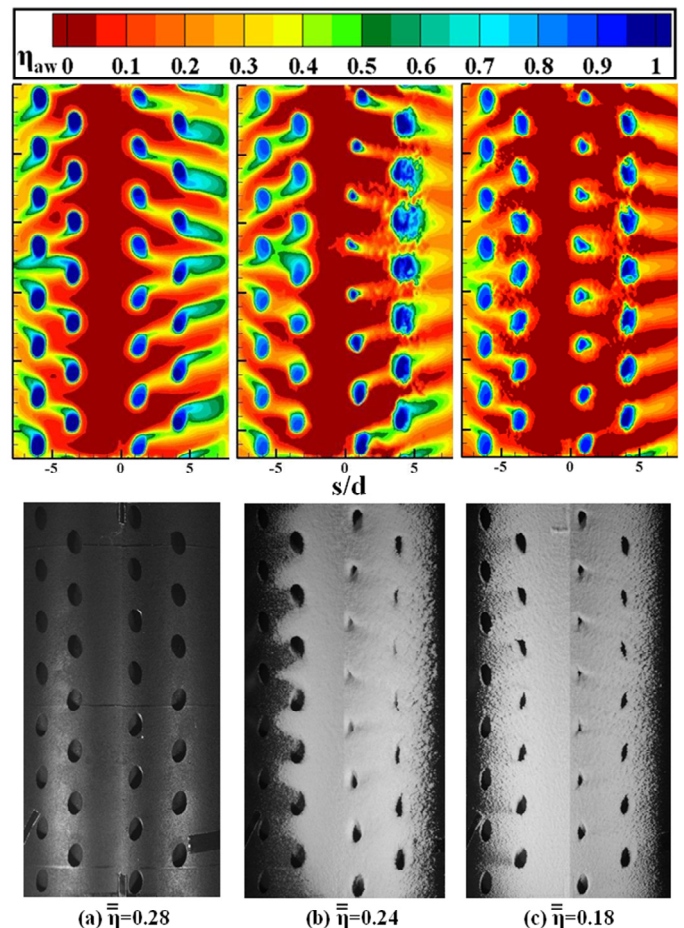

Figure 19. Adiabatic effectiveness contours and deposition photographs for M = 1.0 (a) with no deposition, (b) after 300g at TSP = 1.0 and (c) after 300g at TSP = 2.0.
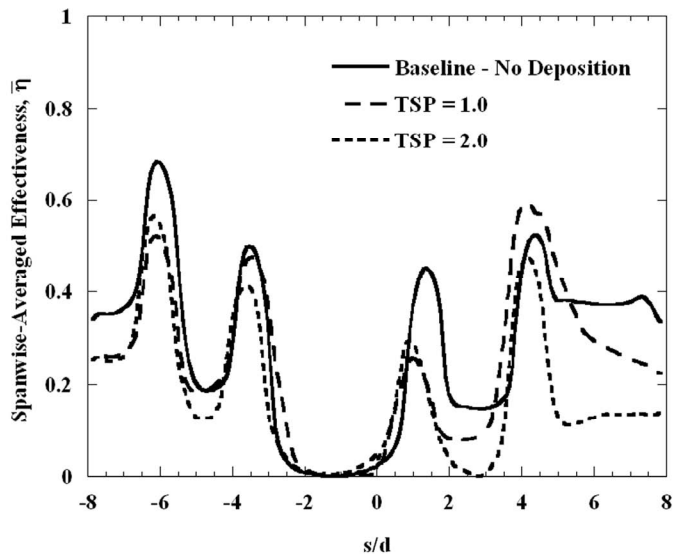
Figure 20. Spanwise-averaged effectiveness plots at M = 1.0 illustrating effects of TSP.

CONCLUSIONS

Deposition was dynamically simulated in a large scale wind tunnel using atomized wax. The effects of wax injection amounts, coolant blowing ratio, and particle thermal scaling parameter on deposition and cooling effectiveness were quantified for a staggered showerhead cooling geometry. Results show that deposition is dependent on cooling condition and the resulting cooling effectiveness is dependent on the deposition on the surface. The two-way coupled relationship makes deposition and its effects on cooling very difficult to predict.

Deposition was simulated at M=1.0 using varying amounts of wax to observe the development of deposition and the effects of deposition development on cooling effectiveness. Deposition thickness measurements showed a linear increase in deposition thickness with the mass of injected wax; however, between 200g and 300g of injected wax, effectiveness reduction changed by less than 2% indicating that effectiveness had reached an equilibrium state.

Cooling effectiveness was quantified before and after deposition at blowing ratios of 0.5, 1.0, and 1.8. Prior to deposition, cooling effectiveness had a peak area-averaged value at M=1.0. At low blowing ratios, cooling near stagnation was insufficient while at high blowing ratios coolant jet separation led to decreased effectiveness. Local blowing ratios were calculated for each row location at each nominal blowing ratio. Results showed that cooling effectiveness increased with an increase in local blowing when $M_L < 1.2$; however, as local blowing ratio exceeded 1.2, coolant jets separated decreasing effectiveness. Deposition simulations revealed that cooling hole blockage decreased with an increase in blowing ratio because increased coolant jet velocity prevented particles from depositing within cooling holes. The thickest deposition occurred downstream of the s/d = 1.2 row at M=1.0 between cooling holes where particles entrained in coolant jets were likely to collect and deposit.

Cooling effectiveness was reduced by deposition at M=1.0 and M=1.8 while deposition led to a slight improvement in

cooling effectiveness at M=0.5. Although area-averaged effectiveness after deposition was highest at M=0.5 than at any other blowing ratio, the coolant coverage near stagnation was most effective at M=1.0 which leads to the conclusion that M=1.0 is the best cooling condition with or without deposition on the surface.

The effects of particle phase on deposition and resulting cooling effectiveness were investigated by simulating deposition at two different mainstream temperatures to achieve thermal scaling parameters of 1.0 and 2.0 at M=1.0. An increase in thermal scaling parameter led to an increase in deposition rate and a dramatic decrease in cooling effectiveness. Although increased combustion temperatures improve the performance of modern gas turbines, the resulting deposition enhanced by the elevated combustion temperatures may lead to critically reduced turbine component life.

ACKNOWLEDGMENTS

REFERENCES

[1] Okita, Y., 2010, Original IHI contract regarding geometric specifications and operating conditions for the staggered showerhead geometry.

[2] Polanka, M.D., Witteveld, V.C., Bogard, D.G., 1999, "Film Cooling Effectiveness in the Showerhead Region of a Gas Turbine Vane Part I: Stagnation Region and Near-Pressure Side," 99-GT-48.

[3] Ou, S., and Rivir, R.B., 2001, "Leading Edge Film Cooling Heat Transfer with High Free Stream Turbulence Using a Transient Liquid Crystal Image Method," *International J. of Heat and Fluid Flow,* **22**, pp. 614-623.

[4] Gao, Z., and Han, J.C., 2009, "Influence of Film-Hole Shape and Angle on Showerhead Film Cooling Using PSP Technique," J. of Heat Transfer, **131** (6), p. 061701 (11 pp.).

[5] Wenglarz, R.A., and Fox, R.G., 1990, "Physical Aspects of Deposition From Coal-Water Fuels Under Gas Turbine Conditions," *J. of Engineering for Gas Turbines and Power,* **112**, pp. 9-14.

[6] Richards, G.A., Logan, R.G., Meyer, C.T., and Anderson, R.J., 1992, "Ash Deposition at Coal-Fired Gas Turbine Conditions: Surface and Combustion Temperature Effects," *J. of Energy for Gas Turbines and Power,* **114**, pp. 132-138.

[7] Wenglarz, R.A., and Wright, I.G., 2003, "Alternate Fuels for Land-Based Turbines," *Proceedings of the Workshop on Materials and Practices to Improve Resistance to Fuel Derived Environmental Damage in Land-and Sea-Based Turbines,* Oct. 22-24, Co. School of Mines, Golden, Co., pp. 4-45 to 4-64.

[8] Smith, C., Barker, B., Clum, C., and Bons, J., 2010, "Deposition in a Turbine Cascade with Combusting Flow," GT2010-22855.

[9] Lawson, S.A., and Thole, K.A., 2009, "The Effects of Simulated Particle Deposition on Film Cooling," GT2009-59109.

[10] Albert, J.E., Keefe, K.J., and Bogard, D.G., 2009, "Experimental Simulation of Contaminant Deposition on a Film Cooled Turbine Airfoil Leading Edge," IMECE2009-11582.

[11] Lawson, S.A., and Thole, K.A., 2010, "Simulations of Multi-Phase Particle Deposition on Endwall Film-Cooling," GT2010-22376.

[12] Sreedharan, S.S., and Tafti, D.K., 2009, "Effect of Blowing Ratio on Syngas Flyash Particle Deposition on a Three-Row Leading Edge Film Cooling Geometry Using Large Eddy Simulations," GT2009-59326.

[13] Lynch, S. P., Sundaram, N., Thole, K. A., Kohli, A., Lehane, C., 2009, "Heat Transfer for a Turbine Blade with Non-Axisymmetric Endwall Contouring," GT2009-60185.

[14] Byerley, A.R., 1989, "Heat Transfer Near the Entrance to a Film Cooling Hole in a Gas Turbine Blade," *D. Phil. Thesis*, Department of Engineering Science, University of Oxford, Oxford, UK.

[15] Meftah, A., Brisard, F., Constantini, J.M., Dooryhee, E., Hage-Ali, M., Hervieu, M., Stoquert, J.P., Studer, F., and Toulemonde, M., 1994, "Track Formation in SiO_2 Quartz and the Thermal-Spike Mechanism," *The American Physical Society, Physical Review B*, **49** (18), pp. 12 457-12 463.

[16] Colban, W., Gratton, A., Thole, K.A., and Haendler, M., 2006, "Heat Transfer and Film-Cooling Measurements on a Stator Vane with Fan-Shaped Cooling Holes," J. of Turbomachinery, vol. 128, pp. 53-61.

[17] Moffat, R.J., 1988, "Describing the Uncertainties in Experimental Results," *Exp. Therm. Fluid Sci.*, **1**, pp. 3-17.